

Prospects for High-Precision Pulsar Timing

K. Liu,^{1,2} J. P. W. Verbiest,² M. Kramer,^{1,2} B. W. Stappers,¹ W. van Straten³
and J. M. Cordes⁴

¹*University of Manchester, Jodrell Bank Centre for Astrophysics, Alan-Turing Building, Manchester M13 9PL, UK*

²*Max-Planck-Institut für Radioastronomie, Auf dem Hügel 69, D-53121 Bonn, Germany*

³*Swinburne University of Technology, PO Box 218, Hawthorn VIC 3122, Australia*

⁴*Astronomy Department, Cornell University, Ithaca, NY 14853, USA*

22 July 2018

ABSTRACT

Timing pulses of pulsars has proved to be a most powerful technique useful to a host of research areas in astronomy and physics. Importantly, the precision of this timing is not only affected by radiometer noise, but also by intrinsic pulse shape changes, interstellar medium (ISM) evolution, instrumental distortions, etc. In this paper we review the known causes of pulse shape variations and assess their effect on the precision and accuracy of a single measurement of pulse arrival time with current instrumentation. Throughout this analysis we use the brightest and most precisely timed millisecond pulsar (MSP), PSR J0437–4715, as a case study, and develop a set of diagnostic tools to evaluate profile stability in timing observations. We conclude that most causes of distortion can be either corrected by state-of-the-art techniques or taken into account in the estimation of time-of-arrival (TOA) uncertainties. The advent of a new generation of radio telescopes (e.g. the Square Kilometre Array, SKA), and their increase in collecting area has sparked speculation about the timing precision achievable through increases in gain. Based on our analysis of current data, we predict that for normal-brightness MSPs a TOA precision of between 80 and 230 ns can be achieved at 1.4 GHz with 10-minute integrations by the SKA. The actual rms timing residuals for each pulsar will be approximately at the same level only if all the other influences on timing precision (e.g. ISM, spin noise) are either corrected, modelled, or negligible.

Key words: methods: data analysis — pulsars: individual (PSR J0437–4715) — ISM: general

1 INTRODUCTION

Pulsars are stable and rapidly rotating radio sources. This stability (which rivals the stability of atomic clocks on Earth, see Hobbs et al. 2010) can be exploited through pulsar timing. In brief, pulsar timing works as follows: after the telescope surface focusses the radio signal at the receiver feed, the signal is amplified, sampled and digitised. Subsequently the frequency-dependent dispersion delay caused by the ionised interstellar medium (ISM) is removed in a process called “de-dispersion”. Then a high signal-to-noise ratio (S/N) pulse profile is obtained by averaging hundreds or thousands of subsequent pulses in a step named “folding”. Finally this high S/N average profile is matched with an independently obtained standard profile (or an analytic template based on the data itself), in order to derive the time-of-arrival (TOA) of the integrated profile.

Precise monitoring of these TOAs allows the investigation of many aspects of the pulsar, the binary system

it inhabits and anything affecting the radio wave propagation. For example, studies of strong gravitational field effects in some binary pulsar systems have in the past enabled some of the most constraining tests of general relativity (Taylor & Weisberg 1989; Kramer et al. 2006). Recent progress in software (e.g. Hobbs et al. 2009) and hardware (e.g. Verbiest et al. 2010) has led to predictions that within a decade, timing of a group of millisecond pulsars (MSPs) will allow various characteristics of a background of gravitational waves to be determined directly (e.g. Jenet et al. 2006; Lee et al. 2008). Furthermore, the next generation of radio telescopes (such as the Square Kilometre Array, SKA, and the Five hundred metre Aperture Spherical Telescope, FAST) will have the best chance of detecting the first pulsar–black-hole binary system (e.g. Cordes et al. 2004). Timing of such a system could determine the spin and quadrupole moment of a black hole and then allow direct tests of the Cosmic Censorship Conjecture and the no-hair

theorem (Kramer et al. 2004). Pulsar timing at very high precision is required to achieve the aforementioned scientific goals, and it is more readily achieved with MSPs because of their short spin periods and highly stable average pulse shapes. Currently, several MSPs have already been timed at precisions down to a few hundred nanoseconds over time spans of a decade or more (Verbiest et al. 2009).

Although the integrated profiles of MSPs appear stable over time scales of years, there are a variety of effects that can affect the shape of an integrated profile on short time scales: multi-path propagation in the turbulent ISM, pulse jitter, data processing artefacts and improper calibration, for example. Profile variations from these effects may only change the pulse shape at low levels, but will cause the subsequent TOA calculation to be less accurate and precise than what is expected if only radiometer noise were contributing to the uncertainty. This will complicate timing with the next generation of radio telescopes since in these cases the timing will be limited by factors other than merely telescope sensitivity.

In order to investigate the level at which short-term instabilities in pulse shape may affect pulsar timing with this new generation of telescopes, we present an analysis on PSR J0437–4715. This pulsar was discovered by Johnston et al. (1993) and is the nearest and brightest MSP known, resulting in outstanding timing precision that has already led to a variety of interesting results (van Straten et al. 2001; Verbiest et al. 2008). Furthermore, the TOA precision of PSR J0437–4715 obtained by current instruments (see e.g. Verbiest et al. 2010) is already comparable to the precision future telescopes may expect to obtain on other less bright MSPs (see Section 5), making it a perfect target for investigations of the pulsar timing potential of future telescopes.

The structure of this paper is as follows. First we describe the observations and data preprocessing in Section 2. Some statistical tools are introduced in Section 3. Next we review the possible effects involved in profile distortion and present the results of data reduction in Section 4. We conclude with an overview of our main findings, prospects for the precision timing with the next generation of radio telescopes, and a brief discussion of future research in Section 5.

2 OBSERVATIONS

The data used in this paper consist of five long observations of PSR J0437–4715, taken between June 2005 and March 2008 at the Parkes radio telescope. Observations were taken with the Caltech-Parkes-Swinburne Recorder 2 (CPSR2; Hotan et al. 2006). The CPSR2 is a 2-bit base-band recorder that performs on-line coherent dedispersion and records two 64-MHz wide observing bands simultaneously. For the data used in this paper, these bands are centred at observing frequencies of 1341 and 1405 MHz. It also effectively removes RFI online by monitoring the total power on μs timescales and does not record any data whenever the power levels deviate significantly from a Gaussian. On two of the five days the data were taken with the H-OH receiver, on the remaining three days the central beam of the 20 cm multibeam (MB) receiver (Staveley-Smith et al. 1996) was used, as listed in Table 1. During each day of observations

Table 1. Basic features of the selected datasets. Note that the 2005-07-24 dataset was used only to create a timing template and a receiver model.

Date	Receiver	Time span (hours)	Number of files	File length (s)
2005-07-24	MB	8.7	1596	16.8
2005-09-07	MB	9.0	1500	16.8
2006-12-31	H-OH	7.4	212	67.1
2007-05-06	H-OH	8.9	152	67.1
2008-02-24	MB	4.0	180	67.1

the data were folded in near-real time to 16.8 s for the early data and to 67.1 s for the later data (see Table 1). Off-source observations of a pulsed noise probe at 45° to the linear feed probes but with otherwise identical set-up, were taken at regular intervals to allow for polarimetric calibration.

For the data processing we used the PSRCHIVE software package (Hotan et al. 2004). We removed 12.5% of each edge of the bandpass to avoid possible effects of aliasing and spectral leakage. Two models named “single axis” and “full reception”, respectively, were used for calibration purposes and details will be presented in Section 4.4. Unless otherwise specified in the text, we combined the polarisations into total power (Stokes I) and the power across the remaining 96 frequency channels. Through the following analysis, TOAs and their uncertainties were determined through the standard cross-correlation approach (Taylor 1992), with the fully integrated 2005-07-24 profiles (one for each observing band), unless otherwise stated. Where needed, we used the timing model derived by Verbiest et al. (2008) without fitting for any parameters.

3 STATISTICAL TOOLS

In order to evaluate any effects on profile shape, we first introduce the concepts of effective pulse number and pulse sharpness below and then briefly illustrate their behaviour with pulse S/N and TOA measurement uncertainty.

3.1 Effective pulse number

As pulsars are weak radio sources and individual pulses are often not detectable, the signal needs to be folded at the rotation period in order to obtain profiles with sufficiently high S/N to derive precise TOAs. It is useful to check whether this procedure is as effective as expected. Theoretically, the signal is expected to increase linearly with integration length, while the root-mean-square (RMS) of the noise increases according to a square-root law. Consequently, the corresponding improvement in S/N is expected to be proportional to the square-root of the number of pulses. Given N profiles with peak amplitudes of A_i and noise RMSs of σ_i ($i = 1, \dots, N$), the single pulse S/N is:

$$(S/N)_i = \frac{A_i}{\sigma_i}, \quad (1)$$

and the S/N of a folded profile is:

$$S/N = \frac{\sum_i A_i}{\sqrt{\sum_i \sigma_i^2}}. \quad (2)$$

If the profiles are identical ($A_1 = \dots = A_N; \sigma_1 = \dots = \sigma_N$), we have $S/N \propto \sqrt{N}$. Practically, however, effects like intrinsic flux variations, scintillation and system temperature variations cause the S/Ns of profiles with identical integration times to differ. This causes deviations from the scaling rule in the processing of real data. Therefore, we define the effective number of pulses as:

$$N_{\text{efc}} = n \left(\frac{S/N}{S/N_{\text{mean}}} \right)^2, \quad (3)$$

where n is the number of pulses within an individual integration, S/N is calculated from Eq. (2), and S/N_{mean} is the averaged S/N for all integrations. Effectively, N_{efc} is a normalised pulse number, which corrects for the varying S/N of individual pulsar pulses. Consequently, the measured S/N of averaged profiles should scale linearly with the calculated $\sqrt{N_{\text{efc}}}$, regardless of the brightness variations of the pulses involved.

3.2 Sharpness and calculation of TOA precision

The main goals of template matching are to calculate the equivalent TOA of the average profile with respect to a fiducial phase provided by the template profile; and to evaluate the corresponding uncertainty caused by the additive noise of the profile. It can be carried out both in the time-domain and (more commonly) in the frequency-domain, by cross-correlating the target profile with a high S/N standard that was either obtained at a different observing time or created analytically (Taylor 1992). Theoretically, the uncertainty of TOA measurements, induced by the white noise of the profile should be in the form of (Downs & Reichley 1983):

$$\sigma_{\text{rn}} = \frac{1}{\beta \cdot S/N_1} \sqrt{\frac{\Delta}{N}}. \quad (4)$$

Here S/N_1 is the equivalent single pulse S/N and

$$\beta = \sqrt{\int [U'(t)]^2 dt} \quad (5)$$

is the pulse sharpness parameter, with $U(t)$ the peak-normalised pulse waveform and

$$\Delta = \int \frac{\langle n(t)n(t+\tau) \rangle}{\sigma_n^2} d\tau \quad (6)$$

is the noise de-correlation time scale where $n(t)$ is the noise function. It can be seen that the sharpness parameter basically relates the intrinsic profile shape to the precision of the TOA.

The template matching technique produces the same result as predicted in Eq. (4), but only if there is no profile shape difference between the template and the observation, which is an ideal assumption in practice. If profile distortion (as can be introduced by any of the effects discussed in Section 4) does occur, the calculated uncertainty does not turn out to be as good as expected for high-S/N profiles. Fig. 1 shows a simulated example of this case. Here a

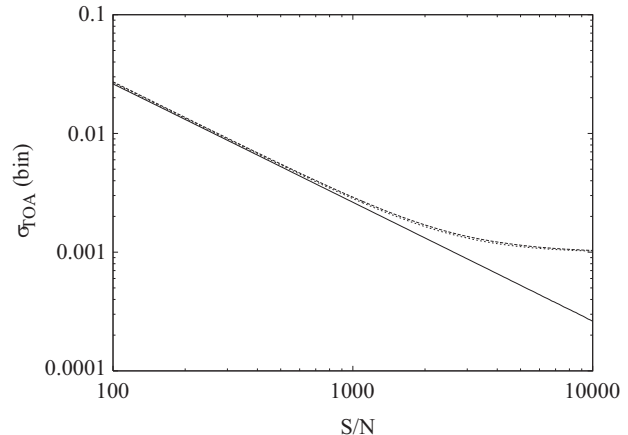


Figure 1. Simulation showing the difference between ideal template matching (solid line) and two cases with profile distortion (dashed line: profile width increased by 0.5%; dotted line: width decreased by 0.5%).

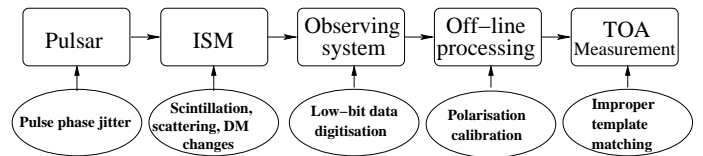


Figure 2. Flow chart of the stages involved in the information transfer of pulsar signals. The corresponding effects that can lead to profile shape changes are identified for each stage.

template is created as a Gaussian and fake observation profiles are formed by adding white noise to the template after being broadened or narrowed by 0.5%. It is clear that the calculated TOA errors begin to deviate from the predicted uncertainty once the S/N rises to values beyond 1000. Note that the deviations are seen to be roughly equal for both the broadened and narrowed cases, which indicates that it is not the absolute pulse shape of the observation determining the reliability of its TOA uncertainty, but the relative difference between the observation and the noise-free template, stressing the importance of reliable template profiles. The different results in the $S/N - \sigma$ graphs presented by Verbiest et al. (2010) and Hobbs et al. (2009) already suggested this to be the case. As their data show, even though the integrated profile for PSR J0437–4715 is supposed to be intrinsically stable at the folding time scale, this phenomenon still appears at high S/N.

4 ISSUES AFFECTING PROFILE STABILITY

In Fig. 2, we summarise the propagation path of pulsar timing data and identify for each stage the phenomena that can affect TOAs and their precision. Some of these are instrumental and correctable while others induce a natural limit to timing precision. Detailed discussions of our current knowledge about these issues together with more in-depth investigations based on our data are presented below.

4.1 Dispersion changes

4.1.1 Theory

The dispersion measure (DM) is defined as the integrated free electron density along the line of sight and introduces a delay between two observing frequencies ν_1 and ν_2 , in the form of (e.g. Lorimer & Kramer 2005)

$$\Delta t \simeq 4.15 \times 10^6 \text{ MHz}^2 \text{ pc}^{-1} \text{ cm}^3 \text{ ms} \times (\nu_1^{-2} - \nu_2^{-2}) \times \text{DM}. \quad (7)$$

There are two ways to correct for this dispersive delay in pulsar timing data. One way is to use a filterbank to split the observing bandwidth up into a finite number of frequency channels, which are subsequently dedispersed with respect to each other. This is called ‘‘incoherent dedispersion’’ because the dispersion is performed post detection when the phase information is no longer available. The alternative approach of ‘‘coherent dedispersion’’ performs a deconvolution on the Fourier transform of the data stream, without loss of frequency resolution (Hankins & Rickett 1975). The coherently dedispersed data is subsequently stored with limited frequency resolution, so any error in the DM value used in the dedispersion, will corrupt the pulse profile permanently.

Because of turbulent motion in the ISM and the relative motions of the pulsar, the Earth and the ISM, the integrated electron density between the pulsar and Earth is continuously changing, implying that ideally the DM value used in on-line coherent dedispersion would be regularly updated to remain close to the current value. Regular updates of the DM values are possible with (near) simultaneous multi-frequency or wide-bandwidth observations (You et al. 2007), but the accuracy of determination by this method is limited by the system sensitivity and complicated by frequency dependent evolution of the profile shape.

4.1.2 Discussion

For the PSR J0437–4715 data used for this paper, given 1024 bins across the profile and a DM of $2.644 \text{ cm}^{-3} \text{ pc}$, the smearing time (see Eq. 7) within a 0.5 MHz wide channel is approximately 0.75 bins. Note that in reality the DM variations of PSR J0437–4715 on long timescales are below $10^{-3} \text{ cm}^{-3} \text{ pc}$ (You et al. 2007), any shape distortion induced by this amount of DM deviation in coherent dedispersion would not be detectable. Therefore, unless the DM variation becomes significantly larger than previously observed, this effect does not affect our current TOA precision. Also note that, since this type of distortion increases the TOA uncertainty by broadening the profile, the uncertainty will still scale following the radiometer equation for future telescopes.

4.2 ISM Scattering and scintillation

4.2.1 Theory

As radio pulses travel through the ionised ISM, multi-path scattering can cause both constructive and destructive interference, observed in the detected signal as apparent brightening and dimming of the pulsar signal. This effect is dependent both on observing frequency and on time because of the relative motion of the pulsar, the Earth and the turbulent ISM. When summing frequency channels of an obser-

vation that is affected by such scintillation, not all frequency channels will contribute equally to the final profile, but effectively a brightness-dependent weighting scheme will be used. In the case where the pulse profile shape varies considerably across the observing bandwidth, such weighting will change the resulting pulse shape as scintles move across the observed bandwidth.

Additionally, multi-path scattering will cause different delays for signals with different path lengths and thereby effectively broaden the observed profile. For low DM sources observed at high frequency, the mean of this profile broadening is non-zero but usually not significant compared with the limited time resolution of the backend (Cordes & Shannon 2010). Still, the change of the pulse broadening function (PBF) associated with either fast, stochastic variations in the diffractive delay, or long-term evolution of the refraction angle, will result in instability of the profile. The pulse broadening will be significantly larger for high DM objects observed at low frequency (Cordes & Shannon 2010). The broadening timescale can be investigated by assuming different scattering models, based on which it is also possible to reveal the intrinsic profile shape by de-convolving the pulse waveform with a theoretical broadening function (Williamson 1973; Bhat et al. 2004; Walker et al. 2008).

4.2.2 Data investigation

The low DM of PSR J0437–4715 ($2.644 \text{ cm}^{-3} \text{ pc}$) corresponds to a short broadening timescale τ_s ($< 10^{-5} \text{ ms}$) and a large decorrelation frequency scale (estimated by $\Delta f \sim 1/(2\pi\tau_s) \approx 0.4 \text{ GHz}$, see Cordes & Lazio 2001; Bhat et al. 2004). Consequently, provided the effective 48 MHz bandwidth¹ of our data, the shape change on short timescales by the PBF variation should be negligible here.

The influence on pulse shape, by the combination of scintillation and profile shape evolution over frequency, can be investigated by dividing the entire bandwidth into sub-bands and carrying out individual template matching. The templates for the sub-bands are produced with the same bandwidth and central frequency as the averaged profiles. Fig. 3 presents an example from the 2005-09-07 dataset. Here the effective bandwidth of 48 MHz is divided into six bands of 8 MHz each. The S/N is calculated from off-pulse bins which show Gaussian statistics. The plot shows that all of the matching processes have identically behaved S/N– σ_{TOA} curves and the same final σ_{TOA} of about 22 ns. Statistically, the six TOAs with an uncertainty of 22 ns each, are equivalent to a single one of uncertainty $22/\sqrt{6} \simeq 9 \text{ ns}$. This is the TOA precision we obtain from template matching the fully frequency-integrated observation. It means that across the 48 MHz bandwidth of this dataset, the TOA precision does not benefit from conducting sub-band template matching. The effect could become significant when the observing bandwidth is comparable to or larger than the scintillation frequency scale. Still, as the effect can be dealt with through the application of frequency-dependent template

¹ As described in Section 2, the total bandwidth is 64 MHz but on either side of the bandpass 12.5% was removed, leaving 48 MHz of effective bandwidth.

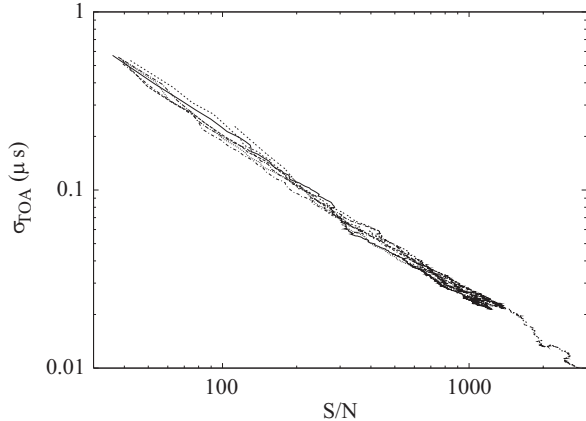


Figure 3. Sub-band template matching for the 2005-09-07 dataset at 1405 MHz. Curves correspond to different bands and the double dashed line is for the entire bandwidth combined. The sub-band curves yield a set of TOAs which are equivalent to a single TOA obtained from the full-band curve.

matching, we conclude that it will not be a limiting factor to TOA precision with either current or future telescopes.

4.3 Signal digitisation effects

4.3.1 Phenomena

Shape distortion induced by instrumental effects obscures the true pulse shape and can therefore be expected to decrease the precision of timing. Two main digitisation effects are pertinent to a low-bit observing system.

The first effect is caused by the underestimation of the undigitised power in a system with low dynamic range (e.g. only 2 bits per sample). As discussed in Jenet & Anderson (1998) (hereafter JA98) the earlier arrival of pulsar emission at the high end of the observing bandwidth causes an increase in undigitised power, and therefore a decrease of the digitised-to-undigitised power ratio at all frequencies if the output power level is kept constant. As a result, the off-pulse power will be decreased in the rest of the band. This effect can be avoided through dynamically setting the output power levels, which provides the required dynamic output range and therefore does not result in negative off-pulse dips on either side of the pulse profile.

The second artefact is caused by quantisation errors as a second-order distortion, and manifests itself as an increase in white noise uniformly redistributed across all frequency channels, which is induced by the increase in pulsed power in one part of the band (JA98). This scattered power broadens the profile and causes additional pulse shape variations as a function of observing frequency, which decreases the achievable TOA precision.

4.3.2 Correction

In this paper, all CPSR2 data presented were corrected for the low dynamic range artefact during on-line processing, by the dynamic output level setting algorithm implemented in

DSPSR² (van Straten & Bailes 2011). The scattered power was mitigated during off-line processing through application of the correction algorithm implemented in PSRCHIVE (Hotan et al. 2004). Given the uncorrected, mean digitized power $\hat{\sigma}^2$ in each pulse phase bin, this algorithm inverts Eq. (A5) of JA98 to estimate the mean undigitised power σ^2 and the mean scattered power A via Eqs. (45) and (43) of JA98, respectively. The effect of correction is demonstrated in Fig. 4, which shows the pulse profile formed from the 2005-07-24 dataset with and without application of the algorithm, as well as the difference between the two. The decreased pulse width of the corrected profile allows higher timing precision. Note that the distortion would not change significantly once the back-end settings are stable. This means that the TOA precision would still scale with effective collecting area as described by the radiometer equation. We therefore conclude that this effect does not limit the current TOA precision, and will not limit it for future telescopes either, which are likely to employ digitisers with a higher number of digitisation levels.

4.4 Polarimetric calibration imperfections

4.4.1 Theory

When a fixed-linear-feed, alt-azimuth radio telescope tracks a polarised source across the sky, the feed will rotate with respect to the plane of polarisation by the parallactic angle (q), which is defined as the angle between the object-zenith great circle and the hour circle. The change of q combined with the instrumental response, will result in a variation of the observed Stokes parameters with time. Polarisation calibration, the aim of which is to reveal the intrinsic profile, will correct this time-dependent variation, but the correction will only be partial if any non-orthogonality of the receptors is not fully modelled. In this case, a difference between profiles at different q will be seen even after calibration. In practice, a “single axis” model considering only the differentials in gain and phase for the two linear polarisation probes is usually applied (e.g. Stinebring et al. 1984). The most recent (here mentioned as “full reception”) model, described by van Straten (2004), solves the matrix description of the polarisation measurement equations, accounting for differential gains and phases, as well as for coupling and leakage effects between the receiver feeds.

4.4.2 Calibration

For comparison, here we used both the “single axis” and the “full reception” model (constructed from the 2005-07-24 dataset) for calibration of the 2005-09-07 dataset. Fig. 5 (a)-(b) shows two hour-long integrated profiles formed from the 2005-09-07 dataset, covering a different range of parallactic angles and calibrated according to the single axis model. The large differences in linear polarisation and position angle demonstrate the imperfection of this calibration model. The difference between the total intensity profile at the two different values of q is shown in subplot (d) of Fig. 5. The same profile as in subplot (a), but calibrated with the

² <http://dspsr.sourceforge.net/>

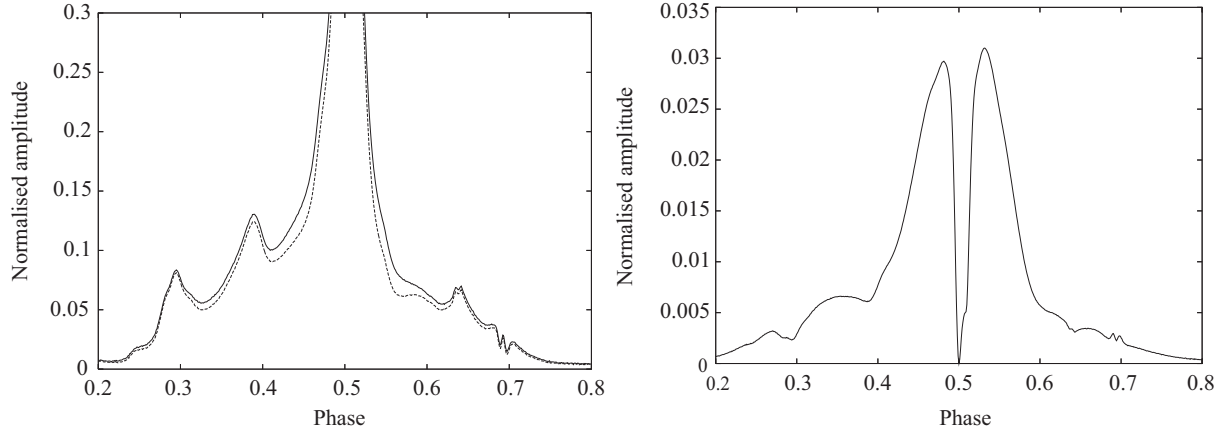


Figure 4. Pulse profiles at 1405 MHz formed from the 2005-07-24 dataset, demonstrating the effect of digitisation scattered power on pulse shape. The left-hand plot shows the zoomed-in pulse profile before (solid line) and after (dashed line) application of the correction algorithm, while the right-hand plot presents the corresponding difference in this phase range, clearly showing the broader shape of the uncorrected profile.

full reception model, is shown in subplot (c) - this profile is identical for both observing times, as the difference plot (e) shows. Furthermore, the profiles calibrated with the full reception model compare well with the previously published polarimetry of Navarro et al. (1997), regardless of q . The remaining difference is clearly far less than 2% of the total intensity, and is therefore below the uncertainty level of the calibration, as quantified through simulations by Ord et al. (2004). Further simulation shows that the profile difference in plot (e) will induce TOA errors of less than 30 ns. It is therefore clear that the full reception model removes all polarisation calibration artefacts down to the level of our current TOA precision on PSR J0437–4715. We hence conclude that polarimetric calibration does not limit the current TOA accuracy above 30 ns. Though the application of these calibration schemes to future interferometers (such as SKA) remains to be solved, such accuracy will be achievable for future single-dish telescopes (such as FAST).

4.5 Interference and unknown observing system instabilities

4.5.1 Diagnostic theory

Besides the expected effects described above, there are some unpredictable effects that may also affect the data quality. Radio frequency interference (RFI) and instrumental failure are the most important two. Specifically in the case of an observing system with only four digitisation levels (i.e. a 2-bit system), any excess in power (as potentially caused by RFI) or a temporary non-linear response in the system, can be expected to affect the pulse shape.

In order to keep track of any such occurrences, the statistics of the digitised data can be compared to those expected from theory, in the following way. First, the digitised data are divided into consecutive segments of L samples and, for each segment, the number of low-voltage states M is counted. The digital signal processing software that is used to process the 2-bit data, maintains a histogram of occurrences of M that is archived with the pulsar data for later use as a diagnostic tool (van Straten & Bailes 2011). When

the voltage input to the digitiser is normally distributed, the ratio $\Phi = M/L$ has a binomial distribution as in Eq. (A6) of Jenet & Anderson (1998). The difference between this theoretical expectation and the recorded histogram of M provides a measure of 1) the degree to which the input signal deviates from a normal distribution, and 2) the degree to which the sampling thresholds diverge from optimality. This difference, called the *2-bit distortion*, is given by

$$D = \sum_{M=0}^L [\mathcal{P}(M/L) - \mathcal{H}(M)]^2 \quad (8)$$

where $\mathcal{P}(\Phi)$ is the expected binomial distribution and $\mathcal{H}(M)$ is the recorded distribution of M . Separate histograms of M are maintained for each polarisation, and the reported distortion is simply the sum of the distortion in each polarisation.

4.5.2 Data analysis

The sharpness parameter can be used to examine profile stability over short lengths of observing time. In Fig. 6, the variations of sharpness and 2-bit distortion (defined in Eq. 8) during the observing runs of 2005-09-07 and 2006-12-31 are shown side by side. Note that the S/N of the individual integrations is typically not sufficient to apply Eq. (5) directly. The sharpness is therefore indirectly obtained through Eq. (4). In doing so, the white noise uncertainty is estimated from cross-correlation with the single integration and the S/N is measured by calculation of the off-peak RMS. As the profile has a large on-pulse duty cycle, only $\sim 15\%$ of the pulse period can be used to calculate the noise RMS, which results in a $\sim 10\%$ uncertainty of both the measured S/N and the sharpness estimates. The 2-bit distortion is calculated by following the stages laid out in Section 4.5.1.

As shown in Fig. 6 the 2-bit distortion levels were consistently low during the 2005-09-07 observation and the sharpness was close to normally distributed. The observation of 2006-12-31, however, shows significantly larger levels of 2-bit distortion as well as correlated, non-Gaussian variations in

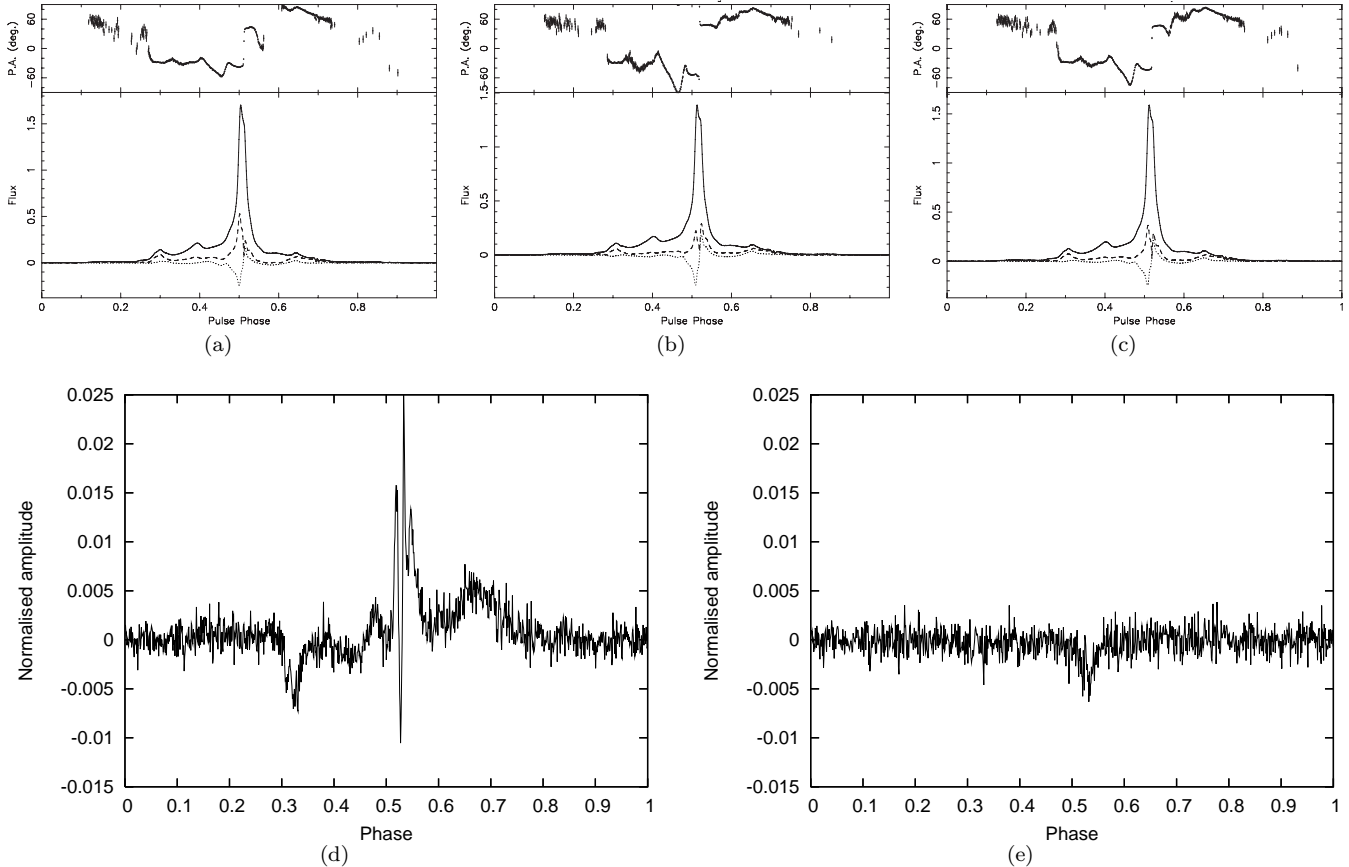


Figure 5. Comparison of polarimetric calibration models. Shown are two hour-long observations from the 2005-09-07 dataset at 1405 MHz at different parallactic angles and calibrated with the single axis (subplots a and b) and full reception models (subplot c, identical for both hours of observations). Here the solid, dashed, and dotted line correspond to the total intensity, linear polarisation, and circular polarisation profiles, individually. The difference of the total intensity profiles for the two hours of observations are shown in subplot (d) for the single-axis calibration scheme and in subplot (e) for the full reception model calibration.

the sharpness parameter. Furthermore, the 2-bit distortion has a high degree of correlation with the sharpness levels. The correlation coefficient of the two time series is -0.73 , suggesting that the profile distortion is related to the digitisation.

To illustrate the effect these digitisation-induced shape changes may have on TOA precision, we provide the $S/N - \sigma_{\text{TOA}}$ plot for the data analysed in Fig. 7. Clearly the 2005-09-07 data behave as expected: they follow the theoretical inverse relationship and worsen slightly for $S/N > 1000$. This worsening is caused by noise in the template profile, which was constructed from the 2005-07-24 dataset. To demonstrate this, we created the $S/N - \sigma_{\text{TOA}}$ curve for simulated data, based on a (simulated) template profile with a S/N identical to that of the 2005-07-24 standard profile. This simulated result is shown as the dotted line in Fig. 7 and follows the 2005-09-07 curve well. Ideally, therefore, a noise-free analytic template profile would be used (as in Kramer et al. 1999), but the small-scale features present in the profile of PSR J0437–4715 require advanced modelling that goes beyond the scope of this paper. This may also explain the flattening of the $\sigma_{\text{TOA}} - S/N$ curve in Verbiest et al. (2010).

The $S/N - \sigma_{\text{TOA}}$ curve for the 2006-12-31 data displays much larger deviations: for equal S/N its TOA uncertainty

(σ_{TOA}) is several factors higher than for the 2005-09-07 data and limits the calculated precision to the ~ 50 ns level.

The other datasets in our investigation (2005-07-24, 2007-05-06 and 2008-02-24) also yield well-behaved $S/N - \sigma_{\text{TOA}}$ curves like that of 2005-09-07, which shows that the majority of our data is not affected by this digitisation artefact. It must be noted that the only objective statistic that we found to clearly identify the 2006-12-31 data as corrupted, was the 2-bit distortion statistic defined by Eq. (8) and that this corruption cannot be corrected post-detection. This demonstrates the need to investigate the digitisation distortion in any 2-bit pulsar timing data and to exclude any distorted data from future pulsar timing analyses. We conclude that these statistics should be used to identify and discard corrupted data. We also note that for systems with more digitisation levels, this type of distortion will not affect TOA precision as much (or at all). It is therefore likely that timing with more state-of-the-art systems on both present and future telescopes, will not be limited by these effects.

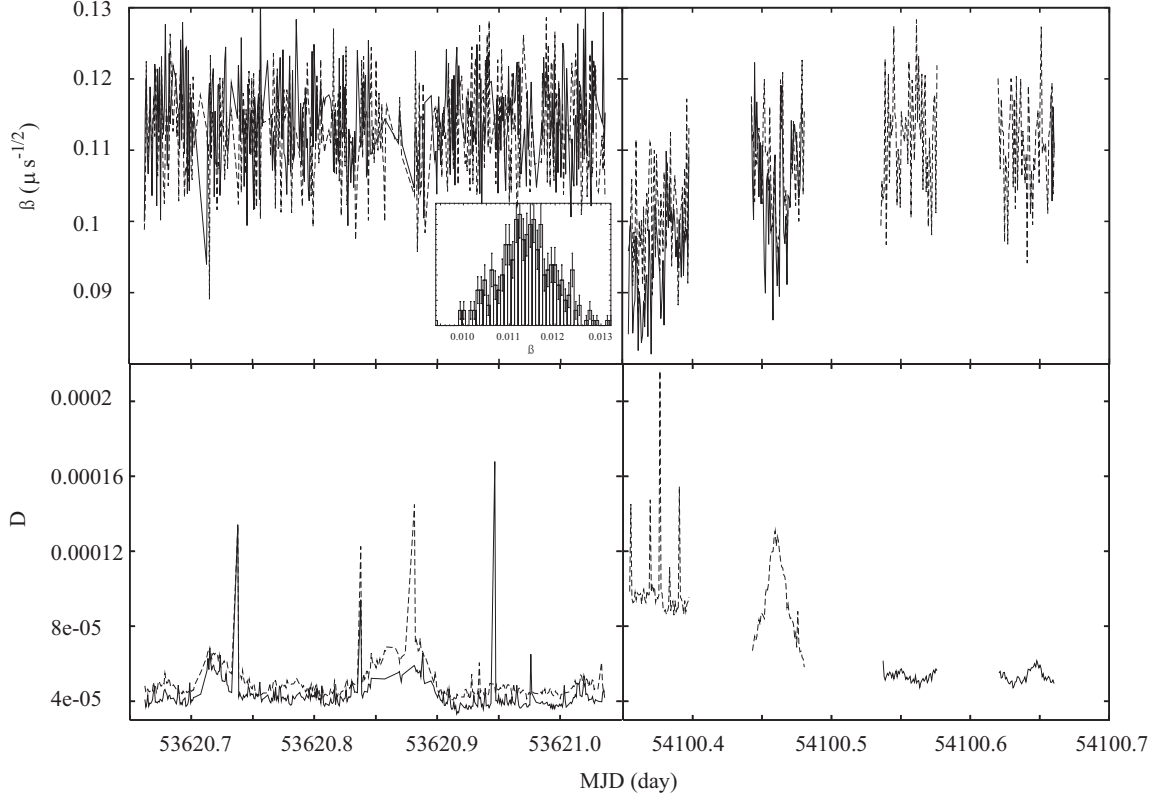


Figure 6. Sharpness β (top) and 2-bit distortion D (bottom) for the observations of 2005-09-07 (left-hand plots) and 2006-12-31 (right-hand plots). Results of the observing band centred at 1405 MHz are shown with solid lines; those of the 1341 MHz observing band with dashed lines. The shape variations on 2006-12-31 identified by the changes in sharpness are clearly correlated with changes in 2-bit distortion, suggesting these variations are instrumental rather than intrinsic to the pulsar. The sharpness variations of the 2005-09-07 data are close to Gaussian as their histogram (inset) shows.

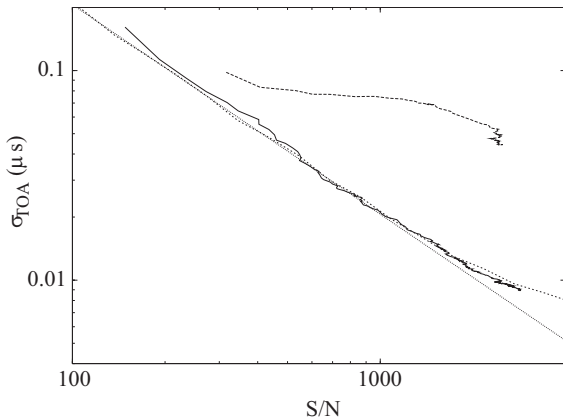


Figure 7. S/N - σ_{TOA} relations for both real data and simulations. The solid line represents the result from the 2005-09-07 dataset, the long-dashed line from the 2006-12-31 dataset. The dotted line shows the theoretical prediction from Eq. (4), and the short-dashed line shows the relationship for simulated profiles cross-correlated with a noisy standard. All these curves are for the observing band centred at 1405 MHz.

4.6 Pulse jitter

4.6.1 Theoretical model

The phases of single pulses vary around an expected, average phase. For some pulsars these phase variations seem random (Ekers & Moffet 1968) and are called “jitter”, while for others there are clearly systematic drifts called “drifting sub-pulses” (Sutton et al. 1970). These phase variations slightly broaden the pulse shape and induce additional arrival phase fluctuation of integrated profiles. For the case of pulse jitter, assuming no modulation of the single pulse shape and intensity, the jitter-induced TOA scatter can be written as (Cordes & Shannon 2010):

$$\sigma_J = \left[\frac{f_J^2 \int U(t)t^2 dt}{N \int U(t) dt} \right]^{1/2}, \quad (9)$$

where N is the number of integrated pulses (assuming no systematic drifting), f_J is the width of the probability density function (PDF) of the phase jitter in units of pulse width, and $U(t)$ is the normalised pulse waveform. Note that this uncertainty is attributed to emission stability of the source and is not related to the observing hardware. One can see that the higher the system sensitivity is, the more important pulse phase jitter may become.

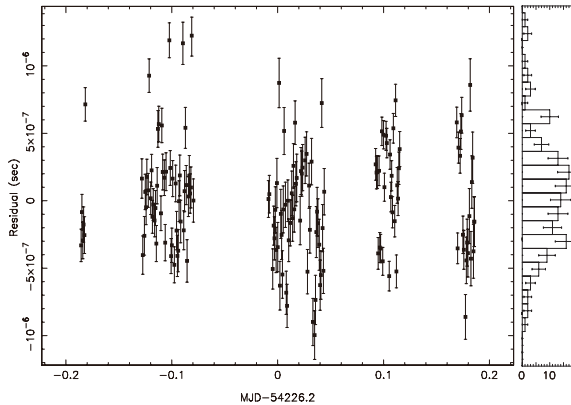


Figure 8. Timing residuals of the 2007-05-06 dataset from the 1405 MHz side-band data. The TOAs derived from 1-min integrations are clearly scattered on a scale larger than the estimated errors with a reduced chi-square of 8.1. The right column shows the histogram of the residuals.

4.6.2 Data analysis

Pulse jitter can be studied by a few methods and in the following we describe each approach in detail.

4.6.2.1 Timing rms The first way to evaluate the impact of pulse phase jitter on timing, is to study the random variations of the TOAs after a timing model has been subtracted. When we consider the timing residuals for the 2007-05-06 dataset, we notice that the TOAs are widely scattered and the reduced chi-square is well above unity (shown in Fig. 8). This is so because the TOA uncertainties have been determined based purely on the amount of radiometer noise in the pulse profile, while other possible contributions of uncertainty such as phase jitter, timing model imperfections, short-term interstellar instabilities and instrumental effects remain unquantified. Note that a previous single pulse study has shown no evidence for pulse drifting (Jenet et al. 1998). The dataset also has passed through the 2-bit distortion test (mentioned in Section 4.5.2) and the residuals satisfy a distribution close to Gaussian, which suggests the insignificance of effects such as faulty ephemeris and improper calibration that can induce non-white noise in timing. The deviation from Gaussian distribution is attributed to both small number statistics, and to differences in measurement precision of the residuals caused by S/N variations in individual integrations. Consequently, we can set up an upper limit on the phase jitter contribution, by assuming that jitter noise is dominant in the additional residual scatter (the amount not quantified by the TOA uncertainties from radiometre noise) and using Eq. (9) to derive the parameter f_J . We find that in this worst-case scenario, $f_J \simeq 0.08$ and $\sigma_{\text{Rad}}/\sigma_J \simeq 0.3$, which means that the timing residuals are dominated by pulse phase jitter and can therefore hardly be improved by increasing the telescope gain, but only by extending the integration time³.

³ The result is consistent for the other datasets and a detailed study will be provided in a subsequent paper

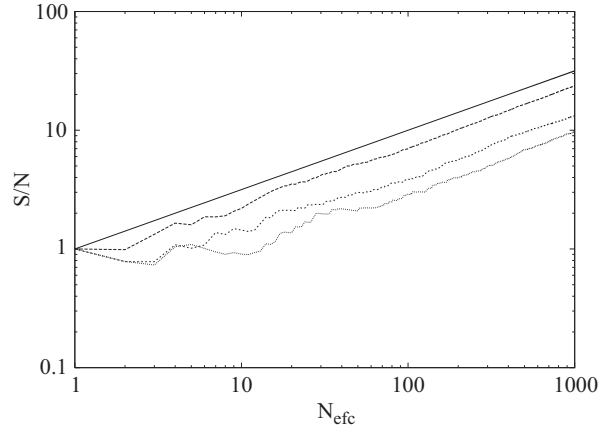


Figure 9. Simulated N_{etc} -S/N curves for both the jitter free and jittered profile cases. The solid, long dashed, short dashed, and dotted lines correspond to jitter factors f_J (see Eq. 2) of 0, 0.1, 0.3 and 0.5, respectively.

4.6.2.2 N_{etc} -S/N relation A second approach to investigate pulse jitter is through the N_{etc} -S/N relation introduced in Section 3.1. A deviation from its theoretical scaling can be induced by inaccurate folding, non-Gaussian noise in the off-pulse baseline or, more interestingly, by pulse jitter. Based on the model of Eq. (9), the effect of pulse phase jitter on the $\sqrt{N_{\text{etc}}}$ -S/N scaling law has been evaluated through Monte-Carlo simulations, as shown in Fig. 9. Here the template of PSR J0437–4715 is used as a single pulse shape, and for each pulse we apply a Gaussianly distributed shift based on a given f_J value. Clearly, the inclusion of pulse phase jitter introduces an initial deviation that is strongly dependent on the value of f_J . After integration of a sufficiently large number of pulses (of the order of a few to several tens of pulses), the scaling law is recovered while the curves remain at a lower S/N than in the jitter-free case. Fig. 10 complements Fig. 9 by plotting the same parameters over a range of increasing integration times. While Fig. 9 shows the simulated effects of pulse phase jitter at the very shortest integration lengths that are inaccessible to our data (which have a minimum length of 16.8 seconds or just under 3000 pulses), Fig. 10 shows the (expectedly stable) behaviour on longer timescales. The S/N_{ref} used for the calculation of N_{etc} is 150, which is roughly the mean value for all 67.1 s integrations. The left plot underlines how the S/N does not scale linearly with the real number of pulses averaged while the right plot does follow the theoretical linear relationship as expected. The phenomenon shown is visible only when the shortest integration time can resolve of the order of ten pulses. These plots do not show any evidence of the effects simulated in Fig. 9. This is to be expected, as the simulations show that the jitter effect saturates after a relatively short integration time, which is not accessible by the (relatively long) integrations of the data we have.

4.6.2.3 Sharpness variation A third diagnostic plot that can be used to analyse pulse phase jitter, is the β - N_{etc} plot. An example of this is provided in Fig. 11, which shows how β converges as more pulses are integrated. This simulation (which was performed in a similar way to that described above) is for the extreme jitter-dominated case. Real

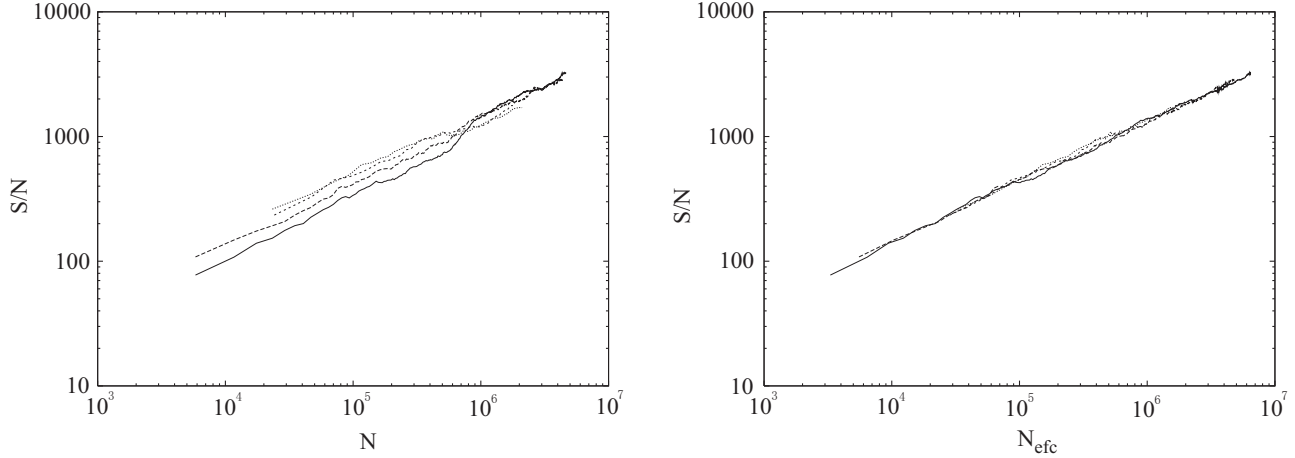


Figure 10. Real and effective pulse number versus S/N, demonstrating the relations between integration time and S/N. These plots are based on data at 1405 MHz from 2005-07-24 (solid line), 2005-09-07 (long dashed line), 2007-05-06 (short dashed line) and 2008-02-24 (dotted line). The theoretical scaling law is clearly reproduced in the N_{eff} graph but not in the true N graph.

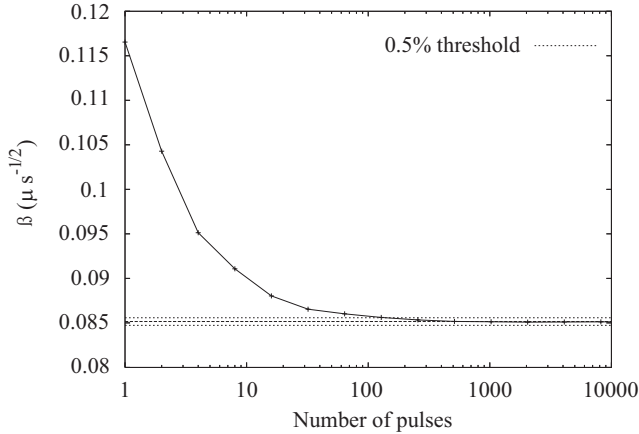


Figure 11. Simulated integration process in the existence of pulse jitter. The profile shape estimated by the sharpness parameter is well constrained below the 0.5 % level after folding of a few hundred pulses. Note that given the rotational period of PSR J0437–4715, 10^4 pulses roughly correspond to an integration time of 1 minute.

data would be a combination of the jitter-induced exponential convergence simulated in Fig. 11 and of Gaussian white noise. However, because the intrinsic shape of single pulses for PSR J0437–4715 is not easily defined, we cannot compare Fig. 11 easily with the β values obtained from our data (as shown in Fig. 6), but we do point out that β does not change significantly as we integrate our data. Furthermore, the variation of β shown in Fig. 6 (top left panel) is far larger than the variation suggested by the simulations (Fig. 11). This suggests either that the simulated level of pulse phase jitter is well below the radiometer noise present in the data, or that there are significant variations in the shape of single pulses, where our model assumes there are none.

4.6.3 Conclusion

In summary, we have used timing measurements to derive the upper limit of $f_J \leq 0.08$ for pulse phase jitter in PSR J0437–4715. This upper limit was subsequently used in simulations to evaluate the impact such jitter would have on the pulse shape and we found that at integration times beyond 100 pulses (~ 0.57 s) neither the S/N of the integrated profile, nor the pulse sharpness are affected significantly compared to the radiometer noise. This lack of pulse jitter effects on the S/N and sharpness of the simulated data, implies either that the derived upper limit is overly conservative and that the underestimation of TOA uncertainties is mostly induced by causes other than pulse phase jitter, or that our model for pulse phase jitter is overly simplistic and a more complex model is required. A more detailed investigation is required to distinguish between these two scenarios and to quantify the pulse phase jitter in PSR J0437–4715 more precisely. Such an analysis is being prepared for a subsequent paper (Liu et al. 2011).

5 DISCUSSION AND CONSEQUENCES FOR FUTURE TELESCOPES

5.1 Summary

In this paper, we have used the brightest and most precisely timed MSP, PSR J0437–4715, to illustrate the most important phenomena known to affect the shape of pulse profiles; to estimate the impact of these phenomena and to evaluate the efficacy of mitigation schemes. By concentrating on the brightest MSP currently known, we are able to cast some light on effects that future telescopes like FAST or the SKA will come across as a matter of course in any standard MSP.

We find that pulse phase jitter may be dominant in current short-term timing of PSR J0437–4715, though further analysis is required to enable quantification of this effect. The effects of faulty de-dispersion are found to be small, negating the need for frequent updates of the dedispersion DM. The effects of scintillation across the bandwidth could not be fully investigated given the limited bandwidth of our

data, but usage of frequency-dependent templates can be expected to resolve the aforementioned problem that scintillation might cause. We present the results of the application of correction algorithms for the most important digitisation artefacts and illustrate the importance of full calibration modelling, as opposed to the more traditional calibration for differential gain and phase only. Finally, we point out the importance of adequate monitoring of the digitisation statistics for 2-bit pulsar observing systems, which is not commonly practised.

We further propose a few diagnostic plots to assess the data quality of any pulsar timing data:

- Time- β curve: Any non-Gaussian variations in profile sharpness suggests changes in pulse shape and imply the data should be carefully studied before being included in any timing analysis (e.g. Fig. 6).
- S/N- σ_{TOA} relation: To assess the quality of the standard profile used (Fig. 1). Deviations from the theoretical relationship or significant differences between datasets indicate data distortion (e.g. Fig. 7).
- S/N- σ_{TOA} for sub-bands: As in the previous point, any mismatch between curves of different sub-bands indicates loss of data quality (e.g. Fig. 3).

Note that the analysis is applicable not only to future telescopes, but also to existing ones such as Parkes, Arecibo, Effelsberg, and the Large European Array for Pulsars (LEAP, see Ferdman et al. 2010), if the system sensitivity is high enough given the brightness of the source.

5.2 Timing in the new millennium

Since PSR J0437–4715 is two orders of magnitude brighter than most MSPs, current observations of this pulsar provide a good demonstration of the TOA measurement situation for most of the MSPs by the next generation of radio telescopes. The 21st century radio telescope will significantly increase the S/N of pulsar detections and correspondingly reduce the uncertainty of TOA measurements through vast increases in effective collecting area.

Fig. 12 shows the expected MSP TOA precision that can be achieved by SKA and FAST. Here for Parkes and FAST we only consider the uncertainty induced by radiometer noise and pulse jitter at the worst-case level derived in Section 4.6.2, while for the prediction of SKA we calculate the upper limit by applying the worst-case in jitter and set up the lower limit by assuming no pulse jitter at all. The instrumental effects causing profile distortions and phase fluctuations are neglected based on previous analyses and the ISM influence on pulse shape is assumed to be either corrected (e.g. Walker et al. 2008) or not significant on a short timescale with provided frequency and bandwidth. Concerning the properties of MSPs, we assume a mean flux density of 3.0 mJy at 1.4 GHz, 50 MHz bandwidth, spin period of 5.0 ms and 5% pulse width. In addition, a 10 K sky temperature at 1.4 GHz is applied. Consequently, it is shown that the TOA precision for normal MSPs can be improved by over one order of magnitude with the next generation of radio telescopes, even when assuming a worst-case level for pulse phase jitter. The result indicates that jitter induced uncertainties will be considerable in future timing of MSPs.

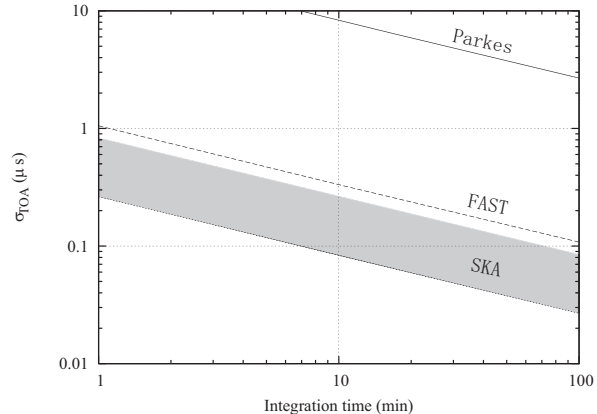


Figure 12. Expected average-brightness MSP TOA scatter versus integration time for different instruments. Only radiometer noise and pulse jitter are accounted for as influences on the measurement accuracy.

Table 2. Key parameters used in prediction of TOA precision for different instruments at 1.4 GHz.

	A_{eff} (m ²)	T_{sys} (K)
Parkes	2.2×10^3	23.5
FAST	7.1×10^4	20.0
SKA core	2.5×10^5	30.0

The instrumental parameters used for these calculations are presented in Table 2 (Schilizzi et al. 2007; Nan 2006).

We conclude that at 1.4 GHz for 10-min integrations, a TOA precision of between 80 and 230 ns can be expected in timing of normal brightness MSPs by SKA. The wide range of this prediction is caused by our limited knowledge of the pulse jitter mechanism. The future radio telescopes will enable deeper investigation of profile stability of single pulses. Presently the comparatively high levels of radiometer noise mean that only a few bright MSPs have allowed a systematic study of their single pulses, where only a subset of the single pulses can be clearly detected (Cognard et al. 1996; Jenet et al. 1998; Edwards & Stappers 2003). The significant improvement in instrumental sensitivity will both dramatically increase the number of MSPs available for single pulse analysis and reduce the selection effects present in current studies.

5.3 Limitations and future work

The analysis based on PSR J0437–4715 is limited by the selected sample. Note that the DM and scattering timescale (see Section 4.2) of this pulsar are relatively low so that the influence of the ISM on the TOA precision within the provided bandwidth is expected to be negligible. As system sensitivity and observational bandwidth are improved, more high-DM sources will be timed at high precision TOA measurements. The effects of scattering and scintillation on profile shape will then become more considerable than shown in this paper, and will need to be accounted for by using

correction algorithms (Bhat et al. 2004; Walker et al. 2008) and/or frequency-dependent template profiles.

ACKNOWLEDGMENTS

We thank A. G. Lyne and M. Purver for their advice and help on this research. The Parkes telescope is part of the Australia Telescope which is funded by the Commonwealth of Australia for operation as a National Facility managed by CSIRO. KL is funded by a stipend of the Max-Planck-Institute for Radio Astronomy. JPWV is supported by the European Union under Marie Curie Intra-European Fellowship 236394.

REFERENCES

- Bhat N. D. R., Cordes J. M., Camilo F., Nice D. J., Lorimer D. R., 2004, *605*, 759
- Cognard I., Shrauner J. A., Taylor J. H., Thorsett S. E., 1996, *457*, L81
- Cordes J. M., Kramer M., Lazio T. J. W., Stappers B. W., Backer D. C., Johnston S., 2004, *The North American Review*, *48*, 1413
- Cordes J. M., Lazio T. J. W., 2001, *549*, 997
- Cordes J. M., Shannon R. M., 2010, arXiv:1010.3785
- Downs G. S., Reichley P. E., 1983, *53*, 169
- Edwards R. T., Stappers B. W., 2003, *Acta Arithmetica*, *407*, 273
- Ekers R. D., Moffet A. T., 1968, *220*, 756
- Ferdman R. D., van Haasteren R., Bassa C. G., Burgay M., Cognard I., Corongiu A., D’Amico N., Desvignes G., Hessels J. W. T., Janssen G. H., Jessner A., Jordan C., Karuppusamy R., Keane E. F., Kramer M., Lazaridis K., Levin Y., Lyne A. G., Pilia M., Possenti A., Purver M., Stappers B., Sanidas S., Smits R., Theureau G., 2010, *Classical and Quantum Gravity*, *27*, 084014
- Hankins T. H., Rickett B. J., 1975, in *Methods in Computational Physics Volume 14 — Radio Astronomy*, Academic Press, New York, pp. 55–129
- Hobbs G., Coles W., Manchester R., Chen D., 2010, arXiv:1011.5285
- Hobbs G., Jenet F., Lee K. J., Verbiest J. P. W., Yardley D., Manchester R., Lommen A., Coles W., Edwards R., Shettigara C., 2009, *394*, 1945
- Hobbs G. B., Bailes M., Bhat N. D. R., Burke-Spolaor S., Champion D. J., Coles W., Hotan A., Jenet F., Kedziora-Chudczer L., Khoo J., Lee K. J., Lommen A., Manchester R. N., Reynolds J., Sarkissian J., van Straten W., To S., Verbiest J. P. W., Yardley D., You X. P., 2009, *26*, 103
- Hotan A. W., Bailes M., Ord S. M., 2006, *369*, 1502
- Hotan A. W., van Straten W., Manchester R. N., 2004, *21*, 302
- Jenet F., Anderson S., Kaspi V., Prince T., Unwin S., 1998, *498*, 365
- Jenet F. A., Anderson S. B., 1998, *110*, 1467
- Jenet F. A., Hobbs G. B., van Straten W., Manchester R. N., Bailes M., Verbiest J. P. W., Edwards R. T., Hotan A. W., Sarkissian J. M., 2006, *653*, 1571
- Johnston S., Lorimer D. R., Harrison P. A., Bailes M., Lyne A. G., Bell J. F., Kaspi V. M., Manchester R. N., D’Amico N., Nicastro L., Jin S., 1993, *Neues Archiv der Gesellschaft für ältere deutsche Geschichtskunde*, *361*, 613
- Kramer M., Backer D. C., Cordes J. M., Lazio T. J. W., Stappers B. W., Johnston S., 2004, *The North American Review*, *48*, 993
- Kramer M., Stairs I. H., Manchester R. N., McLaughlin M. A., Lyne A. G., Ferdman R. D., Burgay M., Lorimer D. R., Possenti A., D’Amico N., Sarkissian J. M., Hobbs G. B., Reynolds J. E., Freire P. C. C., Camilo F., 2006, *314*, 97
- Kramer M., Xilouris K. M., Camilo F., Nice D., Lange C., Backer D. C., Doroshenko O., 1999, *520*, 324
- Lee K. J., Jenet F. A., Price R. H., 2008, *685*, 1304
- Liu K., Keane E. F., Lee K. J., Kramer M., 2011, in preparation
- Lorimer D. R., Kramer M., 2005, *Handbook of Pulsar Astronomy*. Cambridge University Press
- Nan R., 2006, *Science in China G: Physics and Astronomy*, *49*, 129
- Navarro J., Manchester R. N., Sandhu J. S., Kulkarni S. R., Bailes M., 1997, *486*, 1019
- Ord S. M., van Straten W., Hotan A. W., Bailes M., 2004, *352*, 804
- Schilizzi R. T., Alexander P., Cordes J. M., Dewdney P. E., Ekers R. D., Faulkner A. J., Gaensler B. M., Hall P. J., Jonas J. L., Kellerman K. I., 2007, Preliminary specifications for the square kilometre array. Memo 100, SKA Program Development Office
- Staveley-Smith L., Wilson W. E., Bird T. S., Disney M. J., Ekers R. D., Freeman K. C., Haynes R. F., Sinclair M. W., Vaile R. A., Webster R. L., Wright A. E., 1996, *13*, 243
- Stinebring D. R., Cordes J. M., Rankin J. M., Weisberg J. M., Boriakoff V., 1984, *55*, 247
- Sutton J. M., Staelin D. H., R.M. P., Weimer R., 1970, *159*, L89
- Taylor J. H., 1992, *341*, 117
- Taylor J. H., Weisberg J. M., 1989, *345*, 434
- van Straten W., 2004, *152*, 129
- van Straten W., Bailes M., 2011, *28*, 1
- van Straten W., Bailes M., Britton M., Kulkarni S. R., Anderson S. B., Manchester R. N., Sarkissian J., 2001, *Neues Archiv der Gesellschaft für ältere deutsche Geschichtskunde*, *412*, 158
- Verbiest J. P. W., Bailes M., Coles W. A., Hobbs G. B., van Straten W., Champion D. J., Jenet F. A., Manchester R. N., Bhat N. D. R., Sarkissian J. M., Yardley D., Burke-Spolaor S., Hotan A. W., You X. P., 2009, *400*, 951
- Verbiest J. P. W., Bailes M., van Straten W., Hobbs G. B., Edwards R. T., Manchester R. N., Bhat N. D. R., Sarkissian J. M., Jacoby B. A., Kulkarni S. R., 2008, *679*, 675
- Verbiest J. P. W., Bailes M., Bhat N. D. R., Burke-Spolaor S., Champion D. J., Coles W., Hobbs G. B., Hotan A. W., Jenet F., Khoo J., Lee K. J., Lommen A., Manchester R. N., Osłowski S., Reynolds J., Sarkissian J., van Straten W., Yardley D. R. B., You X. P., 2010, *Classical and Quantum Gravity*, *27*, 084015
- Walker M. A., Koopmans L. V. E., Stinebring D. R., van Straten W., 2008, *388*, 1214
- Williamson I. P., 1973, *163*, 345
- You X.-P., Hobbs G., Coles W., Manchester R. N., Edwards R., Bailes M., Sarkissian J., Verbiest J. P. W., van Straten

W., Hotan A., Ord S., Jenet F., Bhat N. D. R., Teoh A.,
2007, 378, 493